

Full-wave electromagnetic modelling of an InP/InGaAs travelling-wave heterojunction phototransistor

To cite this article: Kosmas Tsakmakidis *et al* 2006 *J. Phys. D: Appl. Phys.* **39** 1805

View the [article online](#) for updates and enhancements.

Related content

- [Travelling-wave photonic mixers for increased continuous-wave power beyond 1 THz](#)
Ernest A Michael
- [Analysis on high speed response of a uni-traveling-carrier double hetero-junction phototransistor](#)
Jiang Zhi-Yun, Xie Hong-Yun, Zhang Liang-Hao *et al.*
- [Engineering metallic nanostructures for plasmonics and nanophotonics](#)
Nathan C Lindquist, Prashant Nagpal, Kevin M McPeak *et al.*

Recent citations

- [Analysis on high speed response of a uni-traveling-carrier double hetero-junction phototransistor](#)
Jiang Zhi-Yun *et al*
- [FDTD analysis of slow light propagation in negative-refractive-index metamaterial waveguides](#)
E I Kirby *et al*

Full-wave electromagnetic modelling of an InP/InGaAs travelling-wave heterojunction phototransistor

Kosmas Tsakmakidis, Bernard Weiss and Ortwin Hess

Advanced Technology Institute, School of Electronics and Physical Sciences, University of Surrey, Guildford, GU2 7XH

E-mail: K.Tsakmakidis@surrey.ac.uk

Received 20 September 2005, in final form 3 March 2006

Published 20 April 2006

Online at stacks.iop.org/JPhysD/39/1805

Abstract

Three-dimensional full-wave electromagnetic analysis of a travelling-wave heterojunction phototransistor (HPT) is presented. Employing the finite-difference time-domain method and run on a fast, parallel processing machine the simulation herein allowed, for the first time to our knowledge, the simultaneous investigation of the optical and electrical characteristics of the travelling-wave structure. Snapshots of the field propagation inside the device provide valuable insight into its passive behaviour and conclusively demonstrate the velocity mismatch between the optical wave and the photogenerated electrical signal. Numerical results are presented for the device's output characteristic impedance, photocurrent and effective refractive indices of the optical and electrical signal that quantify the difference in the velocities of the two waves. Moreover, results obtained from the method's initial test in the simulation of an asymmetric planar optical waveguide, similar to the one integrated within the HPT's structure, compare very favourably with the theory.

1. Introduction

The advanced development of telecommunications and the extensive demand for faster and more efficient communication schemes have been of great interest over the past years. Amongst the different systems of communications available and being developed, radio over fibre has proved to be very attractive for backbones in future mobile/wireless systems in terms of bandwidth and cost effectiveness. The potential transmission bandwidth is virtually unlimited and insertion losses are small compared with alternative transmission schemes.

For over two decades, the use of heterojunction phototransistors has attracted the interest of research groups since they combine the functions of photodetection and amplification in a single chip [1–7]. Normal and edge illuminated heterojunction phototransistors (HPTs) have been fabricated and tested, and although remarkable performance has been achieved, the RC time constant limiting factor is still present limiting their usable bandwidth. A travelling-wave (TW) structure where the optical waveguide is coupled into a

coplanar waveguide eliminates this problem by the distributed nature of inductance and capacitance in the structure. This results in high-frequency response limited mainly by the velocity mismatch between the optical wave and the photogenerated electrical signal, as well as by the transit time of the carriers across the absorption region and the mismatch between the characteristic impedance of the electrical equivalent line and the terminating impedance [8–10].

Although such TW-structures have been reported in the literature their development is still ongoing (so far usable bandwidths of some tens of gigahertz have been achieved [11, 12]) and, in order to understand their behaviour, a thorough analysis and modelling are essential. It is the objective of this paper to numerically analyse this type of devices using a general method for numerically solving the time-dependent Maxwell equations in media that is structured on the scale of wavelength. To this end, the finite-difference time-domain (FTD) method was chosen since it has been proved to be very useful and accurate in a variety of applications involving complex electromagnetic structures [13].

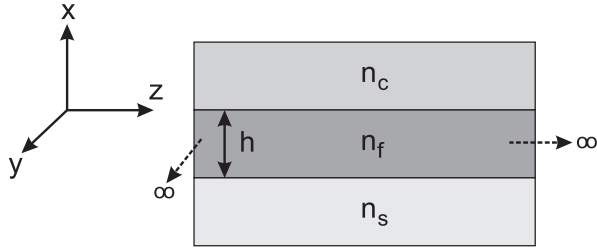


Figure 1. The structure of an asymmetric, planar slab waveguide along with the coordinate system used for its study.

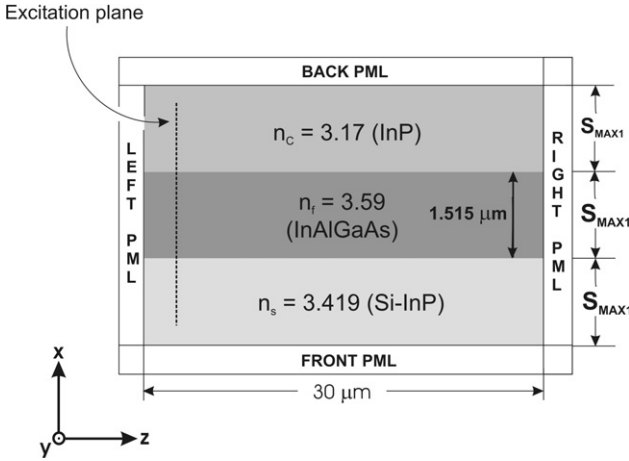


Figure 2. The waveguide/PML geometry used in the FDTD simulations. The conductivity of the PML in each dielectric region, S_{MAXi} , is suitably scaled to maintain a well-posed formulation.

This paper describes the application of the 3D full-wave field-solver to a novel coplanar waveguide (CPW) InP travelling-wave heterojunction phototransistor (TW-HPT) structure and presents numerical results for the output photocurrent, characteristic impedance, electrical losses as well as electrical and optical dispersion. Snapshots of the field propagation inside the device provide useful and illuminating insight into its passive behaviour and clearly demonstrate the velocity mismatch between the optical wave and the electrical signal it generates.

The organization of the paper is the following. The device used herein utilizes a separate waveguide layer made up of quaternary $\text{In}_{0.53}\text{Al}_{0.2}\text{Ga}_{0.27}\text{As}$ material. Its simulation is presented in section 2. Section 3 explains the theory behind the operation of conventional and TW-HPTs, including the structure used in this work. Numerical results and computational details from the FDTD simulation are shown in section 4. Finally, section 5 summarizes the paper presenting the main conclusions of the present study.

2. FDTD simulation of the asymmetric planar slab waveguide

To calibrate and test the accuracy of the method it was first used in the simulation of the asymmetric planar slab waveguide illustrated in figures 1 and 2. The coordinate system that is usually employed for the analysis of optical waveguides [14] is also adopted here for our numerical simulations. The guided eigenmodes in the dielectric heterostructure are

assumed, throughout the following analysis, to travel along the z -axis. This structure is a particular case of an isotropic planar dielectric waveguide that is a crucial part of the travelling-wave phototransistor, as described later in sections 3 and 4.

The waveguide consists of a $1.515 \mu\text{m}$ InAlGaAs film of high refractive index sandwiched between an InP layer (cover) and a Si-doped InP layer (substrate). The optical parameters of each layer for this initial 2D simulation are shown in figure 2. The waveguide length is $30 \mu\text{m}$ and, due to its considerable width (more than $20 \mu\text{m}$), the problem is essentially two-dimensional. For the FDTD simulation, the whole structure is surrounded by a properly modified split perfectly matched layer (PML) in order to accommodate the changes in the refractive indices [15]. Note that, for reasons of comparing the numerical results with closed-form analytical solutions, the absorption coefficient of the i-InAlGaAs layer has not been included in the analysis at this stage but has been incorporated into the 3D field-solver used for the simulation of the TW-HPT, as described later in section 4.

The cell that we used in the FDTD simulations was rectangular, with dimensions $dx = 30 \text{ nm}$ and $dz = 15 \text{ nm}$. The time step was chosen equal to $dt = 0.035 \text{ fs}$, satisfying the Courant stability criterion. The main computational space was composed of 1000×301 cells, while the number of PML cells in the x - and z -axis were 4 and 10, respectively. For excitation we used a Gaussian pulse modulating a sinusoidal carrier. The carrier wave frequency was set to $f_0 = 150 \text{ THz}$ and the full-width at half-maximum (FWHM) was 76 THz . The excitation was applied on the H_y component and the fundamental eigenmode profile was used, which is given by

$$H_y(x) = \begin{cases} A \exp(-\gamma_c x), & x \geq 0, \\ A[\cos(\kappa_f x) - (n_f/n_c)^2 (\gamma_c/\kappa_f) \sin(\kappa_f x)] & -h \leq x \leq 0, \\ A[\cos(\kappa_f h) + (n_f/n_c)^2 (\gamma_c/\gamma_f) \sin(\kappa_f h) \\ \times \exp[\gamma_s(x+h)]] & x \leq -h, \end{cases} \quad (1)$$

where A is the amplitude at the $x = 0$ interface (figure 1) and $\gamma_c, \gamma_s, \kappa_f$ refer to the attenuation coefficients in the cover/substrate and to the transverse component of the wave-vector k in the guiding film, respectively.

By numerically solving the strongly nonlinear characteristic equation for the TM modes [16] for $h = 1.515 \mu\text{m}$ and for the pulse's spectrum central frequency f_0 , we obtained $\kappa_{f0} \cong 1.6154 \times 10^6 \text{ m}^{-1}$, $\beta_0 \cong 1.1162 \times 10^7 \text{ m}^{-1}$, $\gamma_{s0} \cong 3.0364 \times 10^6 \text{ m}^{-1}$ and $\gamma_{c0} \cong 5.0411 \times 10^6 \text{ m}^{-1}$, where the subscript "0" denotes that we are referring to the fundamental mode.

Since the numerical excitation spatially overlaps the desired mode profile very closely, we should expect only this fundamental eigenmode to be excited by the impulsive source [16]. Figures 3(a) and (b) show only one mode being generated which travels along the central dielectric film (z -axis). Moreover, we note that no reflection took place at the left end of the computational space, which confirms the excellent effectiveness of the modified PML.

Finally, based on our 2D-FDTD simulation, we calculated the longitudinal propagation constant β of the fundamental mode as a function of frequency and we compared

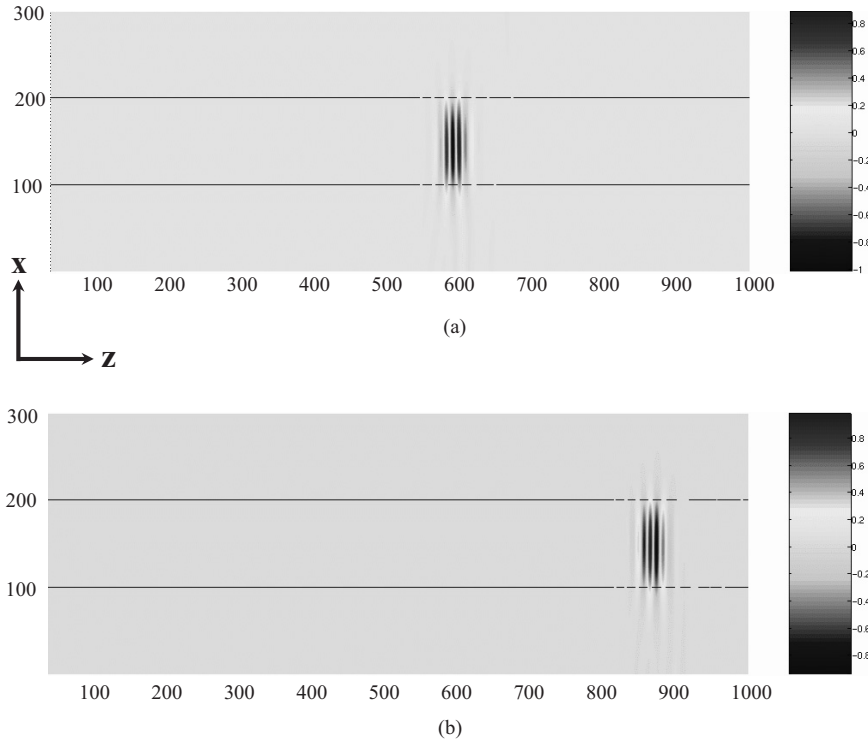


Figure 3. Snapshots of the Gaussian pulse, modulating the sinusoidal carrier, at the time steps (a) $n = 7000$ and (b) $n = 10000$. We note that the pulse is guided along the central film and only a small portion leaks in the surrounding layers. The pulse's leakage in the substrate is also higher due to the smaller difference in the refractive indices between film and substrate rather than between film and cover.

the numerical results with the theoretical values obtained from [17]. The methodology in this analysis [13, 18] is the following: if $V(t, z_i)$ denotes the waveform of an electromagnetic field component at $z = z_i$ and $V(t, z_j)$ is the corresponding waveform at $z = z_j$ then the complex propagation constant $\gamma(\omega) = \alpha(\omega) + j\beta(\omega)$ can be calculated using the relation

$$\gamma(\omega) = \frac{1}{d} \ln \left\{ \frac{\text{FT}[V(t, z_i)]}{\text{FT}[V(t, z_j)]} \right\}, \quad (2)$$

where $d = z_j - z_i$, and $\text{FT}[\]$ denotes the Fourier transform operator. The real and imaginary parts of γ represent field attenuation constant and phase constant, respectively. Any two observation points located along the longitudinal axis of the core can be chosen to record H_y - or E_z - field data as the pulse propagates. Upon dividing the fast Fourier transforms (FFTs) of the two time series and then isolating the imaginary part, β was computed over the frequency range 30–300 THz, as illustrated in figure 4. We note that there is very good agreement between the theoretical and the FDTD-computed results. It is further seen that with increasing frequency, the numerical data start deviating from the exact, theoretical values. This is reasonable since the higher frequencies correspond to smaller wavelengths that cannot be sampled by our space cell as effectively as those that correspond to the lower frequency range of the pulse's spectrum. Therefore, the error is anticipated to increase at higher frequencies.

3. Conventional and travelling-wave heterojunction phototransistors

In a heterojunction phototransistor the exhibited optical gain can be explained via normal bipolar junction transistor (BJT) action. Figure 5 shows the energy band diagram of a conventional HPT and illustrates its operation. The detection of light in this device can be theoretically explained in the following way: the incident light, shown in figure 5, passes unaffected through the wider band-gap emitter and is absorbed in the base, the depletion region between base and collector and in the bulk collector. As can be seen, the photogenerated holes within and close to the base–collector depletion region are easily swept down the potential ‘hill’ and they reach the base region. Because more holes enter the p-doped base region, the forward bias of the base–emitter junction increases. This, in effect, results in the injection of an even larger number of electrons from emitter to base. A significant amount of photocurrent gain can be achieved in this way.

A key feature of an HPT is the use of a wider band-gap emitter. The reason for this is that the emitter injection efficiency can be increased without a corresponding requirement of emitter doping. If we did not employ the conduction-band offset in InP/InGaAs HPTs, it would be necessary to use lightly doped material for the base region (in order to make the ratio i_{nE}/i_{pE} , in figure 5, suitably large) and heavily doped material for the emitter to maintain a high value of its injection efficiency. However, the requirement of light base doping creates a number of problems, such as high base resistance and lateral bias effects, contributing to

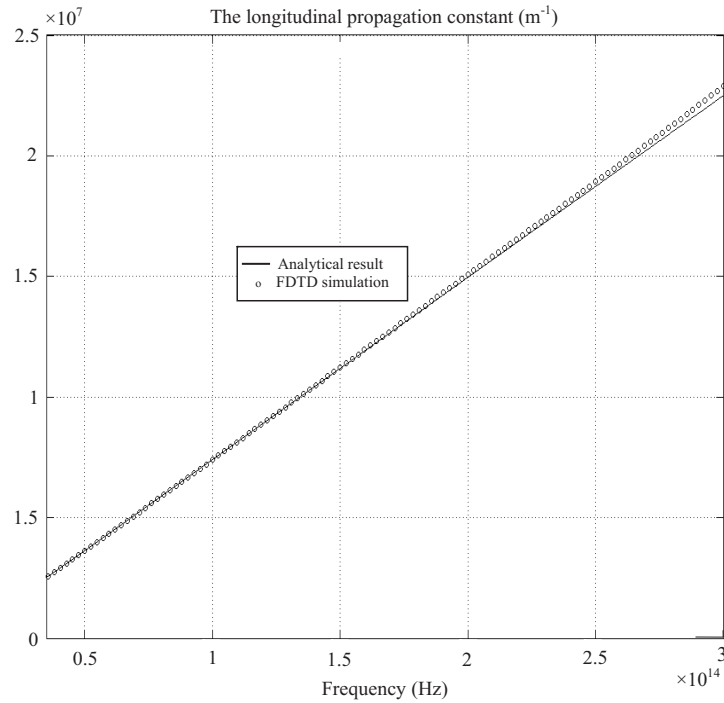


Figure 4. Comparison of FDTD-computed and theoretical values for the propagation constant β of the fundamental TM_0 mode propagating in the optical waveguide under consideration.

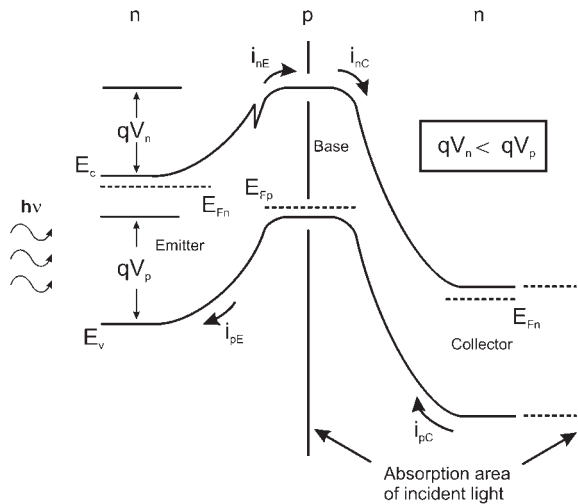


Figure 5. The energy-band diagram of a conventional heterojunction phototransistor (HPT). Also shown are the various current components and the carriers' potential barriers qV_n (electrons) and qV_p (holes).

nonuniform emitter current flow paths, known as ‘emitter crowding effects’, which must be solved by emitter and base contact interdigitation.

From the above discussion it is evident that a more suitable phototransistor for high unit current gain frequency, f_T , would have a heavily doped base and a lightly doped emitter. In an HPT we can achieve that by making the potential barrier for electron injection (qV_n in figure 5) smaller than the hole barrier (qV_p). We can, then, approximate the dependence of carrier

injection across the emitter as [19, 20]

$$\frac{I_n}{I_p} \propto \frac{L_p D_n N_D}{W_b D_p N_A} e^{\Delta E_g/kT}, \quad (3)$$

where N_D/N_A is the emitter/base doping ratio, L_p is the diffusion length of holes in the emitter, W_b is the base width and D_n/D_p is the ratio of electron/hole diffusion constants. For a homojunction phototransistor ΔE_g is zero; hence the improvement factor created by the heterostructure is seen to be $\exp(\Delta E_g/kT)$. This factor is normally quite large in size. For example, if ΔE_g is 0.2 eV and kT is 0.026 eV at room temperature then the factor $\exp(\Delta E_g/kT)$ is about 3000. This allows us to choose the doping characteristics for lower base resistance and emitter–base junction capacitance. In particular, we can choose a heavily doped base to reduce the base resistance and a lightly doped emitter to reduce junction capacitance.

One of the drawbacks that the conventional, lumped-element HPT has is its inability to handle large optical power levels at high-frequency range (above a few tens of gigahertz). This is because in lumped-element HPTs the dimensions of the devices need to be scaled down in order to reduce the transit time that the photogenerated carriers need until they are collected at the two opposite contacts. However, the small devices tend to saturate at low input optical power levels because of small absorption volume [12, 21].

Similarly to the case of photodetectors [8–10], the ‘travelling-wave’ concept has been recently proposed and successfully demonstrated as a means of overcoming the aforementioned problem [11, 12]. In the approach first suggested in [11], light was coupled into a polyamide waveguide sitting on top of the HPT’s active region. While

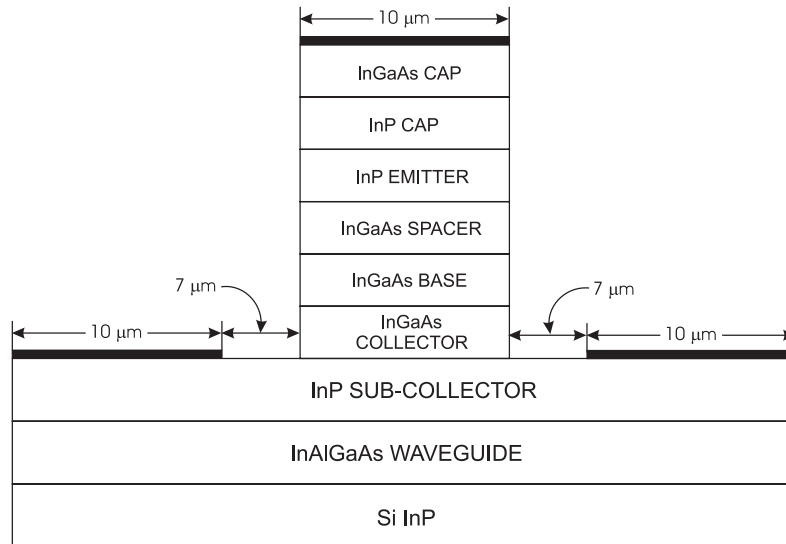


Figure 6. A cross section of the TW-HPT that was simulated with the 3D-FDTD method. The geometrical features of the layers are not drawn to scale. More information about the geometrical and optical properties of each layer is found in section 4 (figure 7 and table 1).

travelling inside the optical waveguide, the optical pulse was absorbed by the lower semiconductor layers (the first of which was the BJT's emitter, as in figure 5) in a distributive way. Electron/hole pairs and a corresponding electrical pulse were, therefore, generated inside the base, base-collector depletion region and bulk collector region, as in a conventional HPT, and optical gain was achieved in a similar fashion with the one that was described at the beginning of the section. Furthermore, similarly to the case of travelling-wave photodetectors (TWPDs), the main bandwidth limitation is due to the velocity mismatch between the optical wave and the photogenerated electrical signal, which suggests that very high bandwidths can be attained with a proper design of the electrical transmission line.

The TW-HPT that was simulated with the FDTD method here is based on an inverted version of the structure reported in [12] and is illustrated in figure 6. In this design the waveguide is embedded inside the semiconductor layer configuration. This allows for a more flexible design since the phototransistor is grown on top of the optical waveguide, allowing for different transistor configurations to be implemented, thereby improving the overall performance of the device and achieving the desired response. Here, the optical waveguide consists of a $1.5 \mu\text{m}$ thick $\text{In}_{0.53}\text{Al}_{0.2}\text{Ga}_{0.27}\text{As}$ layer followed by a thin InP layer, which acts as the sub-collector and ground plane for the electrical waveguide of the structure. The design of the quaternary $\text{In}_{0.53}\text{Al}_{0.2}\text{Ga}_{0.27}\text{As}$ optical waveguide is such that approximately 10% of the guided light is coupled evanescently into the InGaAs base and collector region of the phototransistor. The rest of the device is based on a conventional HPT design [1–7].

4. Full-wave simulation of the travelling-wave HPT

In the following analysis the three-dimensional FDTD-simulation of the travelling-wave heterojunction phototransistor, shown in figure 6, will be described. The geometry of the heterostructure necessitates the use of effective permittivities

Table 1. Permittivity and conductivity data for the layers of the TW-HPT.

	ϵ_r	$\sigma, S/m$
Si InP	12.46	0
InAlGaAs waveguide	12.8881	0
InP sub-collector	12.46	160 200
InGaAs collector	13.88	162.6
InGaAs base	13.88	14 420
InGaAs spacer	13.88	0
InP emitter	12.46	29 480
InP cap	12.46	160 200
InGaAs cap	13.88	253 100

at the interfaces of the dielectrics and ‘special’ schemes for the incorporation of very thin material sheets into the electromagnetic model. Both schemes were used without any instabilities occurring during the time-domain simulation.

We shall begin by showing how the device was “discretized” within FDTD’s framework of analysis and how the formulation of the aforesaid ‘special’ techniques was carried out. We will continue by concisely mentioning the methodology with which important circuit parameters can be obtained from the field-data that FDTD calculates. Finally, snapshots of the field propagation inside the device, as well as numerical results, will provide useful and illuminating insight into the device’s operation and will verify the accuracy and usefulness of our passive numerical analysis.

4.1. Device geometry and FDTD formulation

The device structure and details of the FDTD discretization are shown in figure 7 and table 1 lists the material parameters of each layer. In this study, the cell dimensions were $\Delta x = \Delta y = 0.05 \mu\text{m}$, $\Delta z = 0.1 \mu\text{m}$ and $\Delta t = 0.02 \text{fs}$ was chosen for numerical stability reasons. The Mur absorbing boundary condition (ABC) was applied at the five boundaries of the computational space [13] and the ‘magnetic wall’ was used at the plane $y = 0$. The optical source was a Gaussian pulse with

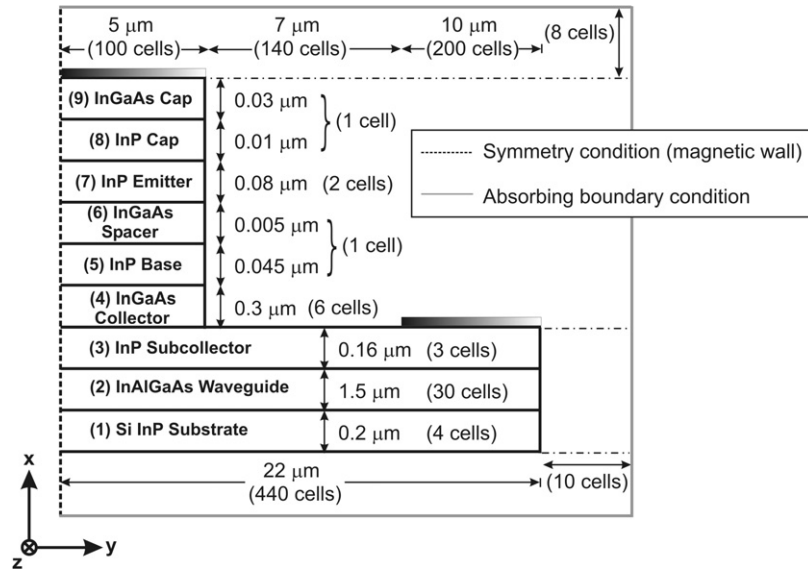


Figure 7. An xy -plane view of the TW-HPT used in the FDTD simulation. Each material layer is given a distinct number for computer-coded reasons. Also, the exact number of cells in this cross-sectional plane is shown.

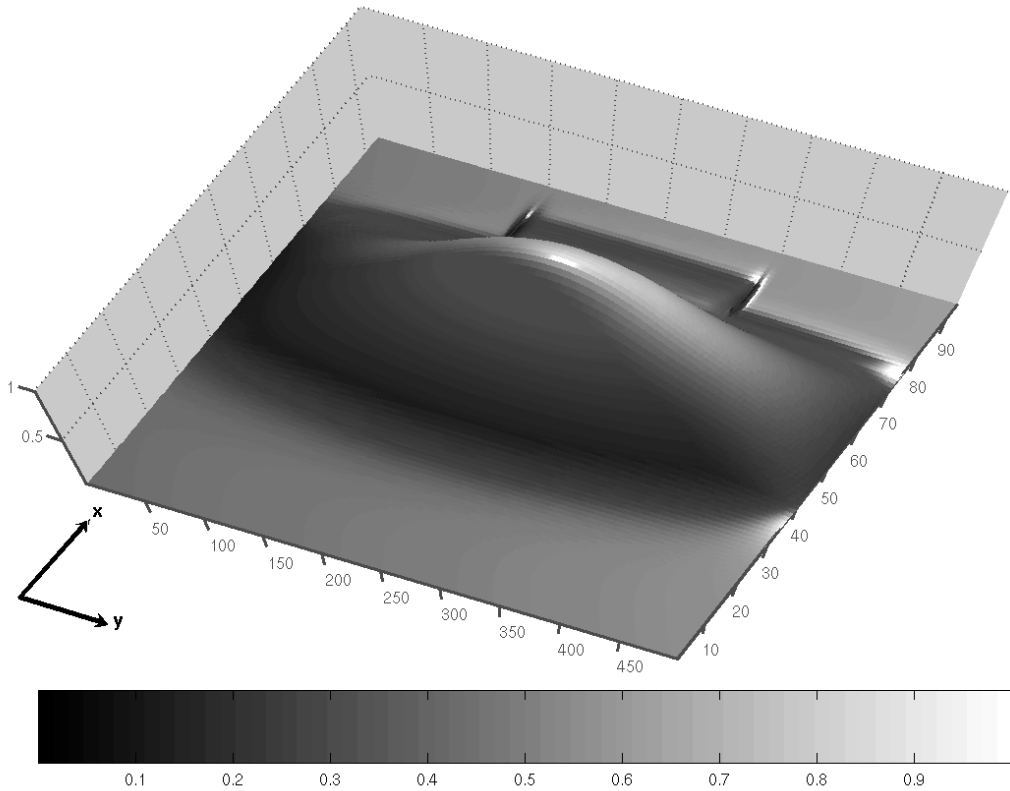


Figure 8. Vertical electric field distribution, E_x , of the fundamental E_x^{11} eigenmode, calculated with the fully-vectorial mode-solver used in [28]. The cross section over which the calculation was made exactly matches that of figure 6. Also shown is the number of grid points in each axis.

parameters $n_0 = 7$ fs, $n_{\text{decay}} = 95$ fs [13] (FWHM 38 THz) and was assigned to the E_x -field components at cells $(i, j) = (24-25, 50-51)$ in the $z = 45$ plane (see figure 7), i.e. light was assumed to be incident from a thin optical fibre, exciting quasi-TM eigenmodes inside the optical waveguide.

For the FDTD implementation, second-order effective permittivity schemes were used at the interfaces of the various

dielectrics (including air) [22]. Furthermore, very thin material sheets InP cap and InGaAs spacer of thicknesses $d_1 = 0.01 \mu\text{m}$ and $d_2 = 0.005 \mu\text{m}$, respectively, were incorporated into the FDTD algorithm without any instabilities occurring. For the sake of brevity, only the values used for averaged permittivity and conductivity in updating E_y and E_z located exactly at the InGaAs cap/InP emitter interface are described in detail and

these are given by

$$\varepsilon_{\text{avg1}} = \left[\left(\frac{1}{2} - \frac{d_1}{\Delta x} \right) \varepsilon_{r, \text{InGaAs}} + \left(\frac{1}{2} + \frac{d_1}{\Delta x} \right) \varepsilon_{r, \text{InP}} \right] \varepsilon_0 \quad (4)$$

and

$$\sigma_{\text{avg1}} = \left(\frac{1}{2} - \frac{d_1}{\Delta x} \right) \sigma_{\text{InGaAs-Cap}} + \frac{d_1}{\Delta x} \sigma_{\text{InP-Cap}} + \frac{\sigma_{\text{InP-Emitter}}}{2}. \quad (5)$$

4.2. Calculation of optical and electrical parameters within the FDTD method

The methodology for the calculation of the usual circuit quantities of voltage, current and impedance from the full-vector E - and H -field distributions in time and space that the FDTD method provides are discussed in [13]. Voltages and currents in the time-domain are obtained by taking the line integral of the electric field between the signal and ground electrodes and by taking the closed integral of the magnetic field around the signal electrode, respectively:

$$V(t, z_i) = \int_{\text{signal electrode}}^{\text{ground electrode}} \mathbf{E} \cdot d\mathbf{s}, \quad (6)$$

$$I(t, z_i) = \oint_{\text{signal electrode}} \mathbf{H} \cdot d\mathbf{s}. \quad (7)$$

The time-domain propagator also allows us to calculate electrical losses and *effective* refractive index of both the optical wave and the electrical signal. The salient features of this methodology are mentioned in section 2, where the derivation of the complex propagation constant $\gamma(\omega)$ is highlighted. As an extension of what we said there, we can define the effective dielectric constant, ε_{eff} , as

$$\varepsilon_{\text{eff}}(\omega) = \frac{\beta^2(\omega)}{\omega^2 \mu_0}, \quad (8)$$

based on which the effective refractive index versus frequency can be obtained

$$n_{\text{eff}}(\omega) = \left[\frac{\varepsilon_{\text{eff}}(\omega) \mu_r}{\varepsilon_0} \right]^{1/2}. \quad (9)$$

Equations (2) and (9) can be used for both the optical wave and the electrical signal depending on whether the fixed observation points are inside the optical or the electrical waveguide. Thus, numerical results for the absorption of the optical field, electrical losses and the group velocities of the two waves can be promptly obtained.

4.3. Simulation results and discussions

The 3D-FDTD simulation enables us to consider passive-layer absorption, non-degenerate leaky mode-coupling [12], electrical and optical dispersion and velocity mismatch all together. In the microwave photonics area and for the simulation of photodetectors in particular [23, 24], the usual approach for source modelling is to define a photocurrent source at specific grid points. In this manner, regardless of the optical waveguide properties, the presence of propagating optical waves is incorporated into the FDTD algorithm by

means of photogenerated current density in the transverse direction that is produced by photogenerated carriers given by

$$J_{\text{transverse}}(z) = \frac{q\lambda}{hcW_i} \Gamma \alpha_0 P_0 e^{-\Gamma \alpha_0 z}, \quad (10)$$

where q is the elementary charge, W_i the width of the signal electrode, Γ the optical confinement factor, α_0 the optical power absorption coefficient and P_0 the incident photon flux. Similarly, in commercial simulation packages, such as ATLASTM device simulation software of Silvaco [25], a photogeneration rate is defined at each grid point along the ray path, based on which an expression similar to (10) is derived for photocurrent density. While this approach is valid and can lead to accurate results for lumped-element photodetectors, it is not immediately appropriate for a TW structure because it does not directly allow for the possibility that more modes than one may propagate along the optical waveguide. When the planar dielectric waveguide is not single-mode, this results in the number and nature of excited optical modes, e.g. with a usual butt-coupling approach, not being included in the analysis [26]. Therefore, the optical power distribution in the direction of current flow, hence the spatial variation of electron/hole pairs generation, cannot be properly accounted for.

In order to simulate the propagation of the optical wave in such a structure, the source (usually Gaussian) must be assigned to one of the electric or magnetic field components inside the optical waveguide and the bandwidth of the excitation pulse should be well within the optical range of the signal spectrum [27]. More importantly, the very small wavelengths present in the simulation domain necessitate the use of even smaller cell-dimensions for the compensation of numerical dispersion [13]. This is the reason for using a large 3D space lattice ($60 \times 250 \times 450$ cells, figure 7) composed of very small cells (maximum dimension $0.1 \mu\text{m}$) in the FDTD simulation. Moreover, the several tens of thousands of time steps needed to fully evolve the device's impulse response and to acquire the necessary frequency-domain information mean that we need to resort to a supercomputer, in order to run the simulation in a reasonable amount of time (typically several hours).

A preliminary simulation of the 3D rectangular optical waveguide was carried out to identify and monitor the location where the maxima of the first two E_x modes occurred, since in the present dynamical model the modes are not formed instantaneously. It was found that almost all field energy was launched into these two modes. In the 3D FDTD simulation of the TW-HPT, *each* mode inside the i -layer, conveying field energy, $J_{\text{source-}j}$, ($j = 1, 2$) [13] was then allowed to decay with distance, z , according to (10). The absorption coefficient was fixed to $7 \times 10^3 \text{ cm}^{-1}$ [26] and the optical power confinement factor for the two modes was $\Gamma_1 = 0.97627$ and $\Gamma_2 = 0.93627$, calculated first with the effective-index method and refined afterwards with a robust fully-vectorial mode-solving technique [28]. An exemplary result of this calculation, showing the distribution over the TW-HPT's cross section of the dominant component of the E_x^{11} eigenmode, is illustrated in figure 8. Particularly for the quantitative investigation of the velocity mismatch between optical and electrical waves, such an approach is essential and sufficient.

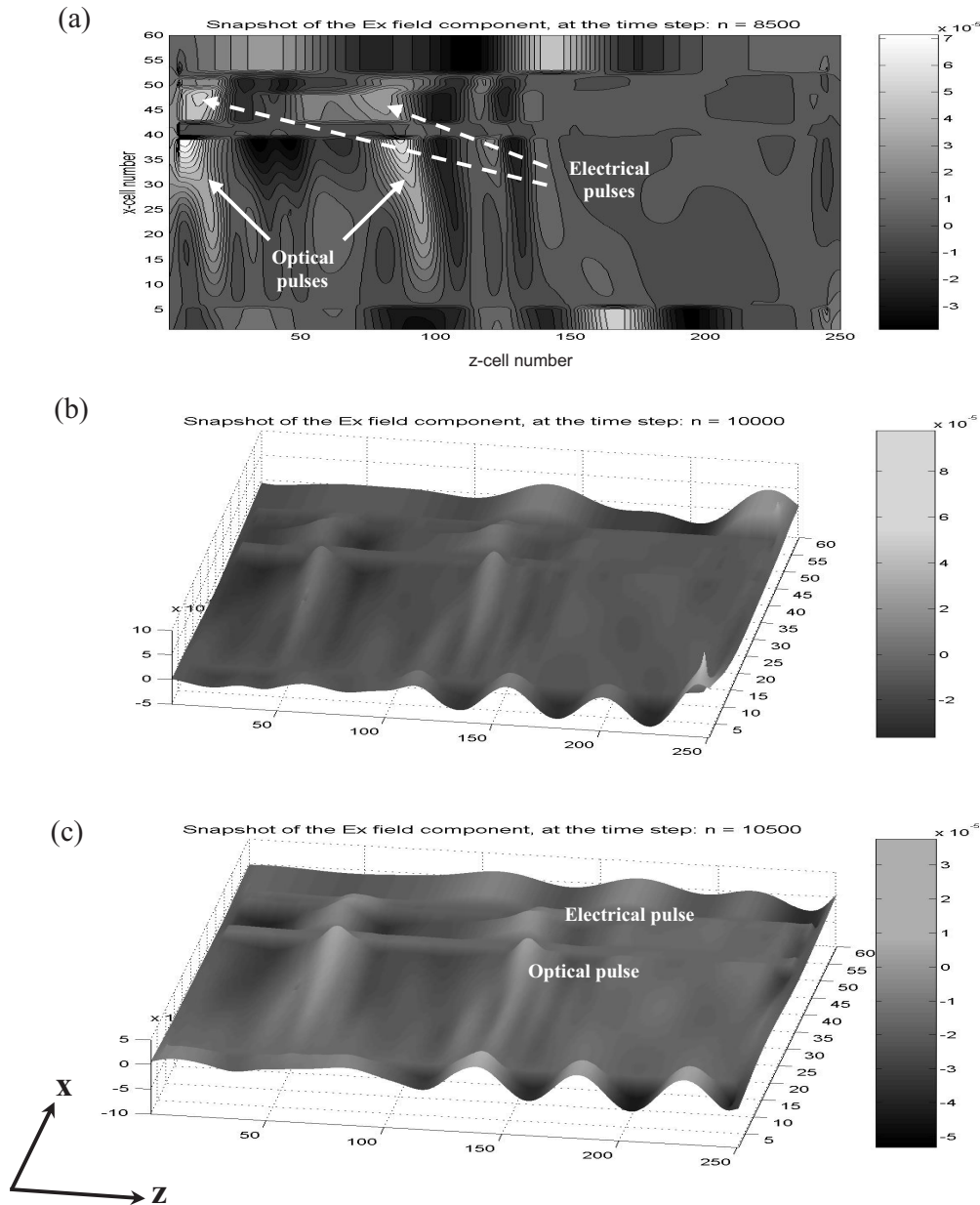


Figure 9. Snapshots of the E_x -field spatial distribution at the $z = 51$ plane at three time steps. (a) This clearly shows the presence of two pairs of pulses; the pulses on the left hand are about to be reflected. (b) In this snapshot the pulses have been reflected. In practical TW-HPTs, a reverse termination is usually used to absorb the electrical signal travelling in the reverse direction. (c) Studying the right-hand pair of pulses, the electrical pulse clearly lags significantly owing to velocity mismatch.

Figure 9 illustrates three successive snapshots of the E_x spatial distribution at the plane $z = 51$, which is perpendicular to the middle of the central metallic strip of figure 7. The layout of the device is clearly seen in figure 9(a), with the InP sub-collector separating the optical and electrical waves. These snapshots conclusively demonstrate the velocity mismatch between the optical and the photogenerated electrical pulse, the split of the electrical pulse into two equal parts travelling in opposite directions and the resulting waste of 50% of the photocurrent (if the reverse wave is terminated). The reflection of the electrical wave at the device's input results in two components for the total current. Figure 10 shows the extracted effective refractive indices for the optical and electrical waves. It is found that $n_{\text{opt.}} \cong 3.01$ and $n_{\text{elect.}} \cong 3.2$, which agree with

the visual evidence of velocity-mismatch shown in figure 9. Note that, herein, the velocity mismatch between the optical wave and the electrical transmission line is smaller than the one reported in [12], calculated there at $1.3 \mu\text{m}$ free-space wavelength.

Based on the methodology mentioned in section 4.2 the 3D-FDTD model was further applied for the calculation of photocurrent at various cells along the HPT (z -axis), as illustrated in figure 11. The simulation correctly predicts the attenuation of the photocurrent's amplitude with distance owing to microwave losses. It is seen that while the major current-pulse propagates through the top metallic contact its amplitude decreases mainly because of electromagnetic energy loss to conducting electrons. It also broadens out owing

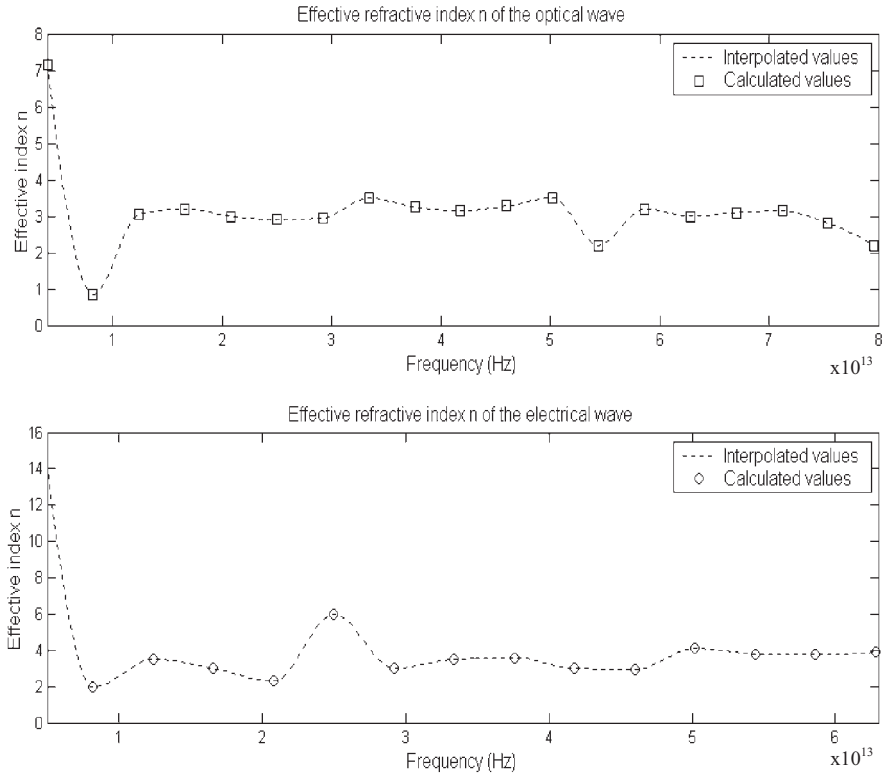


Figure 10. Effective refractive indices of the optical and electrical waves. There is a dc-offset in low frequencies and the peaks are due to multimodal propagation.

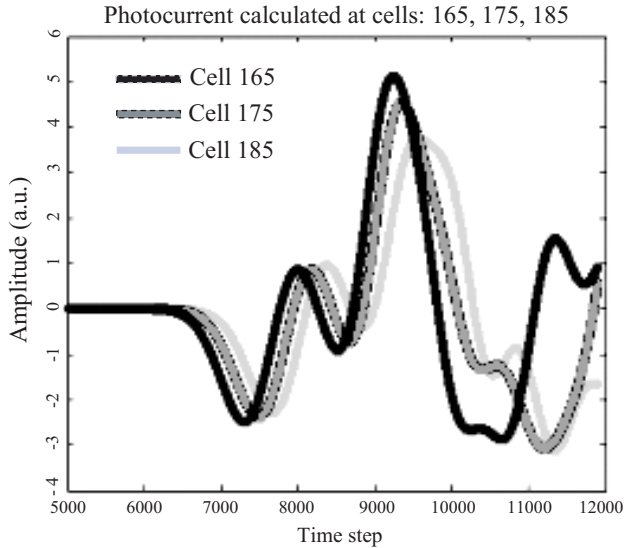


Figure 11. Photocurrent at three different cells along the y-axis; shown here is the recorded result between time steps $n = 5000$ and $n = 12000$.

to electrical dispersion. The current-pulses behind and in front of the main pulse are due to contributions from optical modes other than the dominant one, which propagate along the optical waveguide, as was seen in figure 9, and which would have otherwise been ignored in other analytical or simulation approaches.

Finally, the characteristic impedance (Z_0) versus frequency of the device is calculated and shown in figure 12.

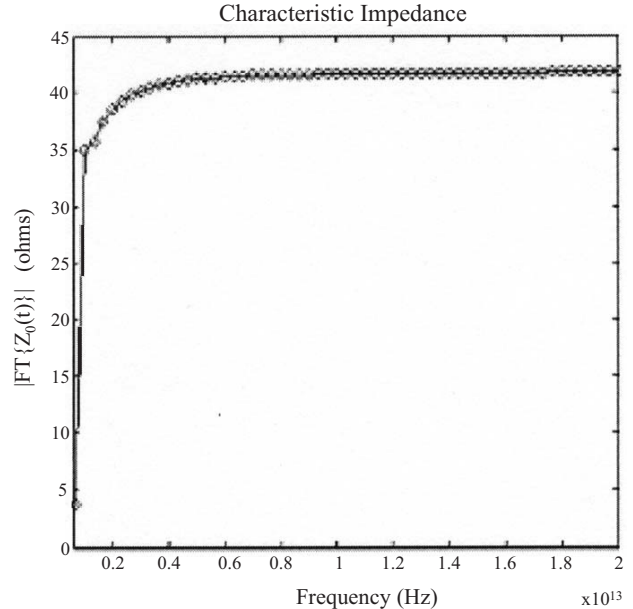


Figure 12. The amplitude of the characteristic impedance at cell 185 versus frequency. Note the characteristic "dc-offset" in the low-frequency range.

It is found that the amplitude of Z_0 is constant (around $42\ \Omega$) over the frequency range of the excitation pulse, thereby providing a good impedance matching to an external $50\text{-}\Omega$ circuit. At the low-frequency range the results, as expected, deviate from the exact values due to 'dc-offset' [13].

5. Conclusions

Full-wave time-domain analysis of the performance of a travelling-wave heterojunction phototransistor has been presented. A three-dimensional electromagnetic model of a TW-HPT, enhanced with effective permittivity schemes and special techniques for the incorporation of thin material sheets, has been constructed, capable of indicating main device characteristics including optical absorption, electrical losses, as well as optical and electrical dispersion.

Run on a parallel-processing machine, the numerical model provided useful and illuminating insight into the device's passive behaviour and conclusively demonstrated the velocity mismatch between the optical wave and the electrical signal it generates. The split of the input optical pulse into two equal, oppositely travelling pulses was revealed from the results of the simulation. Each one of the pulses generated an electrical pulse and an accompanying current component. Finally, we observed the reflection of the optical and electrical waves at the device's input that, as is known from the device's theory, results in two components for the total current.

Acknowledgments

The authors would like to thank Professor I D Robertson (University of Leeds) and Dr L Gomez-Rojas for useful discussions and Professor P A Houston and his team (University of Sheffield) for the provision of the TW-HPT's design and their cooperation. They also gratefully acknowledge financial support of the Engineering and Physical Sciences Research Council (EPSRC), UK. Finally, the authors would like to express their sincere gratitude to the anonymous reviewers for their constructive comments, which enhanced the quality of the paper.

References

- [1] Milano R A, Dapkus P D and Stillman G E 1982 An analysis of the performance of heterojunction phototransistors for fibre optic communications *IEEE Trans. Electron Devices* **29** 266–74
- [2] Sasaki A, Yano H, Fujita S and Takeda Y 1985 Integrated optical devices of InGaAsP/InP heterojunction phototransistor and inner stripe light-emitting diode *J. Lightwave Technol.* **3** 1264–9
- [3] Wake D, Newson D J, Harlow M J and Henning I D 1993 Optically-biased, edge-coupled InP/InGaAs heterojunction phototransistor *Electron. Lett.* **29** 2217–9
- [4] Van de Castele J, Vilcot J P, Gouy J P, Mollot F and Decoster D 1996 Electro-optical mixing in an edge-coupled GaInAs/InP heterojunction phototransistor *Electron. Lett.* **32** 1030–2
- [5] Liu C P, Seeds A J and Wake D 1997 Two-terminal edge-coupled InP/InGaAs heterojunction phototransistor optoelectronic mixer *IEEE Microw. Guided Wave Lett.* **7** 72–4
- [6] Kamitsuna H, Matsuoka Y, Yamahata S and Shigekawa N 2001 Ultrahigh-speed InP/InGaAs DHPTs for OEMMICs *IEEE Trans. Microw. Theory Tech.* **49** 1921–5
- [7] Magnin V, Van de Castele J, Vilcot J P, Harari J, Gouy J P and Decoster D 1997 A three-terminal edge-coupled InGaAs/InP heterojunction phototransistor for multifunction operation *Microw. Opti. Technol. Lett.* **17** 408–12
- [8] Giboney K S, Rodwell M J W and Bowers J E 1997 Traveling-wave photodetector theory *IEEE Trans. Microw. Theory Tech.* **45** 1310–19
- [9] Giboney K S 1995 Traveling-wave photodetectors *Ph.D. Thesis* Department. Electrical and Computer Engineering, University of California at Santa Barbara
- [10] Shi J W and Sun C K 2000 Design and analysis of long absorption-length traveling-wave photodetectors *J. Lightwave Technol.* **18** 2176–87
- [11] Prakash D P, Scott D C, Fetterman H R, Matloubian M, Du Q and Wang W 1997 Integration of polyimide waveguides with traveling-wave phototransistors *IEEE Photon. Technol. Lett.* **9** 800–2
- [12] Scott D C, Prakash D P, Erlig H, Bhattacharya D, Ali M E, Fetterman H R and Matloubian M 1998 High-power high-frequency traveling-wave heterojunction phototransistors with integrated polyamide waveguide *IEEE Microw. Guided Wave Lett.* **8** 284–6
- [13] Taflove A and Hagness S C 2000 *Computational Electrodynamics: the finite-difference time-domain method* (Boston/London: Artech House Publishers)
- [14] Marcuse D 1974 *Theory of Dielectric Optical Waveguides* (New York: Academic)
- [15] Reuter C E, Joseph R M, Thiele E T, Katz D S and Taflove A 1994 Ultra-wideband absorbing boundary condition for termination of waveguiding structures in FD-TD simulations *IEEE Microw. Guided Wave Lett.* **4** 344–6
- [16] Pollock C 1995 *Fundamentals of Optoelectronics* (Homewood, IL: Irwin)
- [17] Kogelnik H and Ramaswamy V 1974 Scaling rules for thin-film optical waveguides *Appl. Opt.* **13** 1857–62
- [18] Liang G C, Liu Y W and Mei K K 1989 Full-wave analysis of coplanar waveguide and slotline using the time-domain finite-difference method *IEEE Trans. Microw. Theory Tech.* **37** 1949–57
- [19] Streetman B G and Banerjee S 2000 *Solid state electronic devices* (Upper Saddle River, NJ: Prentice Hall)
- [20] Casey H C and Panish M B 1978 *Heterostructure Lasers -Part A: Fundamental Principles* (London/New York: Academic)
- [21] Lin L Y, Wu M C, Itoh T, Vang T A, Muller R E, Sivco D L and Cho A Y 1997 High-power high-speed photodetectors—design, analysis, and experimental demonstration *IEEE Trans. Microw. Theory Tech.* **45** 1320–331
- [22] Hwang K P and Cangellaris A C 2001 Effective permittivities for second-order accurate FDTD equations at dielectric interfaces *IEEE Microw. Wirel. Compon. Lett.* **11** 158–60
- [23] Kong S-C, Lee S J, Lee J-H and Choi Y-W 2002 Numerical analysis of traveling-wave photodetectors' bandwidth using the finite-difference time-domain method *IEEE Trans. Microw. Theory Tech.* **50** 2589–97
- [24] Kong S-C, Ok S-H, Choi Y-W, Choe J-S, Kwon Y-H and Kim J-H 2003 Numerical analysis and design of a new traveling-wave photodetector with an asymmetric i-layer cross section *IEEE J. Sel. Top. Quantum Electron.* **9** 770–5
- [25] Atlas User's Manual 2000 *Device Simulation Software I* (Santa Clara: Silvaco International)
- [26] Allsopp D W E, Stern M S, Strobel E 1999 Analysis of edge-coupled heterojunction phototransistors *IEEE Trans. Microw. Theory Tech.* **47** 1289–96
- [27] Tsakmakidis K L, Gomez-Rojas L, Robertson I D, Hess O, Houston P A and Weiss B 2004 FDTD modeling of velocity mismatch in traveling-wave heterojunction phototransistor *Electron. Lett.* **40** 452–4
- [28] Tsakmakidis K L, Hermann C, Klaedtke A, Jamois C and Hess O 2005 Systematic modal analysis of 3-D dielectric waveguides using conventional and high accuracy nonstandard FDTD algorithms *IEEE Photon. Technol. Lett.* **17** 2598–600